Cross power spectral density based beamforming for underwater acoustic communications

Jianghui Li[a], Yechao Bai[b], Youwen Zhang[c,*], Fengzhong Qu[d], Yan Wei[d], Junfeng Wang[e]

[a] *Institute of Sound and Vibration Research, University of Southampton, Southampton SO17 1BJ, U.K.*
[b] *The School of Electronic Science and Engineering, Nanjing University, China.*
[c] *The College of Underwater Acoustic Engineering, Harbin Engineering University, Harbin, China.*
[d] *Ocean College, Zhejiang University, China.*
[e] *the School of Electrical and Electronic Engineering, Tianjin University of Technology, China.*

Abstract

In underwater acoustic (UWA) communications, beamforming is often used to improve the detection performance of a receiver. For beamforming, there have been methods presented in time domain, e.g., fractional delay (FD) method, and in frequency domain, e.g., time-frequency-time with cross spectral density matrix (TFT-CSDM) method. The former brings accurate direction of arrival (DOA) estimation but with high complexity and is vulnerable to noise; while the latter brings less accuracy but with lower complexity. In this paper, we propose and investigate a time-frequency-time with cross power spectral density (TFT-CPSD) beamforming method for a vertical linear array (VLA) of hydrophones. The proposed method is compared with the FD and the TFT-CSDM methods in a receiver designed for guard-free orthogonal frequency-division multiplexing (OFDM) with superimposed data and pilot signals. The comparison is based on data obtained in sea trials at distances 30 km to 50 km in the northwest Pacific Ocean. The results demonstrate that the proposed TFT-CPSD method possesses higher accuracy than the TFT-CSDM method, and lower complexity than the FD method. Besides, the OFDM receiver with the TFT-CPSD beamforming outperforms a receiver with the TFT-CSDM beamforming and the FD beamforming at signal to noise ratio (SNR) from -14 dB to 14 dB. The proposed beamforming technique possesses the merits of energy conservative and energy leakage reduction, which can also be applied to single-carrier transmission.

Keywords: `Beamforming; cross power spectral density (CPSD); direction of arrival; orthogonal frequency-division multiplexing (OFDM); underwater acoustic communications`

1. Introduction

In underwater acoustic (UWA) communication channels, ambient noise (e.g., radiated from sea surface wave agitation, shipping, snapping shrimps, etc.) is one of the dominant factors that affects the performance of data transmission [1, 2, 3, 4, 5, 6, 7]. To reduce such negative effect and improve the signal to noise ratio (SNR), receivers with vertical linear arrays (VLAs) have been developed associated with using different beamforming techniques, and are currently used in UWA communications [8, 9, 10, 11].

In the past decades, these beamforming techniques have been verified as of providing significant improvement in the detection performance of a receiver [12, 10]. Typically, these beamforming techniques involve steps of estimating direction of arrival (DOA), and applying such estimates to produce angle-specific directional signals for equalization and demodulation [8, 9]. The result of DOA estimation reveals the detection accuracy, and the angle-specific directional signals usually possess higher SNR than the data received directly from the acoustic channel.

There have been beamformed techniques presented in two ways, i.e., in time domain, and in frequency domain. Time domain beamforming techniques have been proved as possessing high accuracy, but they usually need to conduct interpolation operation between data samples, which results in high computational complexity. Moreover, such interpolation may lead to energy leakage [13], especially at

*Corresponding author: Youwen Zhang

low SNRs, which can reduce the detection accuracy of a DOA estimator and the detection performance of a receiver.

To reduce the complexity and remove the beamforming leakage, a frequency domain low complexity beamforming was presented in [10], which is known as time-frequency-time (TFT) beamforming. Such TFT beamforming firstly divides the received data packet into multiple frames, transforms the data frames from time domain to frequency domain, computes cross spectral density matrix (CSDM) for each frame in frequency domain thus providing weights to improve the beamforming performance, and finally transforms the frequency domain signal back to the time domain. Such process avoids the time domain interpolation thus reducing the computational complexity. However, such TFT beamforming applies the CSDM to compute the beamformer weights, which does not provide strong weights to the DOA as the computation of CSDM does not fully reveal the energy of data received from all directions. As a result, the accuracy of DOA estimator based on it has been presented as significantly inferior to that of the interpolation based fractional delay (FD) beamforming [8, 10].

The continuous time domain process of the FD beamforming does not need to separate a continuous received signal into blocks, which avoids information loss and interference from the tail with delayed signals between blocks. However, the interpolation used in such time domain process can result in high computational complexity. Besides, it may introduce another issue of beamforming energy leakage revealing at specific directions, especially at low signal-to-noise (SNR), which will be investigated in this work.

A beamforming technique is usually tested at various SNRs by adding noise from the channel. However, the underwater ambient noises on different receive hydrophone channels have been usually assumed as uncorrelated and Gaussian distributed [14, 15, 16, 17, 18, 19, 20]. This assumption makes the data processing simple but may not be the case in real ocean scenarios and may change the capacity of channel spatial modulation [21], e.g., the beamforming.

In this paper, we propose and investigate a beamforming algorithm, which provides high accuracy of DOA estimation for UWA communications utilizing a receive VLA of hydrophones. The proposed beamforming method computes cross power spectral density (CPSD) to estimate the beamforming weights. The investigation is based on sea trials with guard-free orthogonal frequency-division multiplexing (OFDM) signals received by a 14-element VLA of hydrophones [22, 23]. The sea trials were conducted in the northwest Pacific Ocean, with a transducer towed by a vessel moving at speeds of 8 m/s and 3 m/s, at 30 km and 50 km away from the receive VLA, respectively. In the sea trials, the DOA estimator using the proposed TFT-CPSD beamforming shows higher accuracy than the TFT-CSDM beamforming and lower complexity than the FD beamforming. Besides, the receiver using the proposed TFT-CPSD beamforming outperforms that of using the FD beamforming and the TFT-CDSM beamforming at SNRs from -14 dB to 14 dB. Further, we verify low beamforming energy leakage of the proposed beamforming method while showing high DOA estimation accuracy by using the Waymark propagation model simulation [24, 25].

The paper is organised as follows. Section 2 describes the transmitted signal and the receiver. Sections 3 describes the spatial filter used in the receiver, and the three beamforming techniques used in the spatial filter. Section 4 compares the accuracy of DOA estimator utilizing the beamforming techniques. Section 5 compares performance of the receiver with the three beamforming techniques using sea trial data. Section 6 uses the Waymark model based simulation to verify low energy leakage from the proposed beamforming. Section 7 summarizes the paper with discussion.

2. Transmitted signal, and receiver

In this section, we consider the guard-free OFDM signals as the transmission signal, as its ability to cope with severe underwater channel conditions without complex equalization filters. The equalizer used in the receiver here is based on that presented in [23]. The receiver composes a spatial filter, in which the proposed beamforming algorithm is implemented.

2.1. Transmitted signal

The transmitted signals $\mathrm{s}(t)$ consists of L guard-free OFDM symbols with superimposed data and pilot signals [23], with each OFDM symbol given by:

$$\mathrm{s}_l(t) = \Re\left\{ e^{j2\pi f_c t} \sum_{k=-N_s/2}^{N_s/2-1} [M_1(k) + jD_l(k)] e^{j\frac{2\pi}{T_s}kt} \right\}, \tag{1}$$

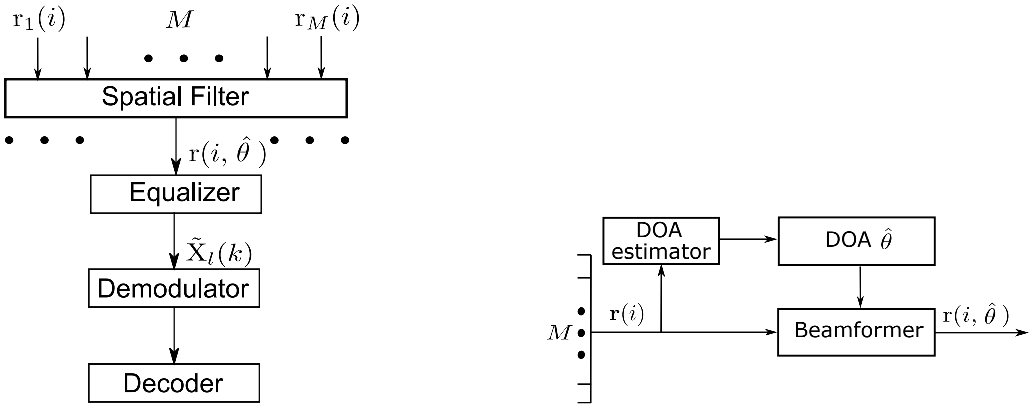

(a) receiver

(b) spatial filter

Figure 1: (a) Block diagram of the receiver; M is the number of hydrophone channels [10]; see [23] in detail. (b) Block diagram of the spatial filter.

where $\Re\{\cdot\}$ denotes the real part of a complex number, $N_s = 1024$ is the number of sub-carriers, $f_c = 3072$ Hz is the carrier frequency, $T_s = 1$ s is the symbol duration resulting a subcarrier spacing of 1 Hz, and $j = \sqrt{-1}$. The sequence $M_1(k) \in \{-1, +1\}$ is a binary pseudo-random sequence of length N_s, serving as the pilot signal. The binary sequence $D_l(k)$ represents the information data in the lth symbol, $l = 1, 2, \ldots, L$, which is obtained by encoding and interleaving the original data across sub-carriers using 1/2 rate convolutional code [26].

2.2. Receiver

Fig. 1(a) shows the block diagram of the receiver. The analogue signals received by M hydrophones are bandpass filtered within the frequency bin of the OFDM transmission and converted into the digital form $\mathrm{r}_1(i)$ to $\mathrm{r}_M(i)$ at a sampling rate f_s, i being the discrete time index; $f_s = 4f_c = 12288$ Hz in this case. The digital signals $\mathrm{r}_1(i)$ to $\mathrm{r}_M(i)$ are processed in a spatial filter that produces directional signals. In this paper, we only consider the directional signal with the highest power (see [10] for maximum ratio combining technique of multiple directional signals), denoting it as $\mathrm{r}(i, \hat{\theta})$. The DOA $\hat{\theta}$ is chosen from the average signal power as a function of received angle. The directional signal is Doppler estimated and compensated, and then equalized in time domain [23], and transformed into the frequency domain using the fast Fourier transform (FFT). The frequency domain signal $\tilde{\mathrm{X}}_l(k)$ is transferred to a demodulator and, after deinterleaving, further to the soft-decision Viterbi decoder [27] (see [10] for details).

3. Spatial filter

Fig. 1(b) shows the block diagram of the spatial filter used in the receiver. The DOA estimator computes the spatial power distribution to estimate DOA. Then, the beamformer uses the DOA estimate to produce the directional signal $\mathrm{r}(i, \hat{\theta})$.

In the spatial filter, the following three beamforming techniques are considered:

- the FD beamforming [8, 10] (Section 3.1);
- the TFT-CSDM beamforming [10] (Section 3.2);
- the proposed TFT-CPSD beamforming (Section 3.3).

3.1. Fractional delay (FD) beamforming

Spatial filter using FD beamforming provides accurate DOA estimation but has high complexity [10]. To achieve the high accuracy when processing wideband signals, such as communication signals, both the DOA estimator and beamformer should operate by introducing delays (fractional delays with respect to the sampling interval) in the hydrophone signals. The pseudo code for the FD beamforming is shown in Algorithm 1.

Algorithm 1 Fractional delay (FD) beamforming

Require: hydrophone positions, received data package $\mathrm{r}_m(nT)$ at each hydrophone m, $n = 1, 2, \ldots, N$;

procedure
  for each interested direction θ **do**
    compute delay $\varsigma(m, \theta) = \frac{\mathrm{D}(m)\sin(\theta)}{c}$
    compute $M \times N$ snapshot matrix $[\mathbf{X}(\theta)]_{m,n} = \mathrm{r}_m(nT - \varsigma(m, \theta))$
    calculate sample covariance matrix $\mathbf{R}(\theta) = \mathbf{X}(\theta)\mathbf{X}^T(\theta) + \kappa\mathbf{I_M}$
    compute spatial signal power $\tilde{\mathrm{P}}(\theta) = \left[\sum_{m=1}^{M}\sum_{n=1}^{M}[\mathbf{R}^{-1}(\theta)]_{m,n}\right]^{-1}$
  end for
  find maximum power $P_{\max} = \max_\theta \tilde{\mathrm{P}}(\theta) \rightarrow \hat{\theta}$ ▷ DOA estimation
  compute weight factor $\tilde{\mathrm{w}}(\hat{\theta}) = \tilde{\mathrm{P}}(\hat{\theta})\left[\sum_{n=1}^{M}[\mathbf{R}^{-1}(\hat{\theta})]_{1,n}, \ldots, \sum_{n=1}^{M}[\mathbf{R}^{-1}(\hat{\theta})]_{M,n}\right]^T$
  beamformed signal $\mathrm{r}(i, \hat{\theta}) = \left[\mathbf{X}^T(\hat{\theta})\tilde{\mathrm{w}}(\hat{\theta})\right]_i$ ▷ beamformed signal
end procedure

3.1.1. FD DOA estimator

In the FD beamforming, the $M \times N$ snapshot matrix $\mathbf{X}(\theta)$ for a specific direction θ is used for calculating the diagonally loaded sample covariance matrix [8]

$$\mathbf{R}(\theta) = \mathbf{X}(\theta)\mathbf{X}^T(\theta) + \kappa\mathbf{I_M}, \tag{2}$$

and

$$[\mathbf{X}(\theta)]_{m,n} = \mathrm{r}_m(nT - \varsigma(m, \theta)), \; n = 1, 2, \ldots, N, \tag{3}$$

where $(\cdot)^T$ denotes the transpose, $\mathbf{I}_M$ is an $M \times M$ identity matrix, and κ is a loading factor which is a small positive number used here to prevent numerical instability. In our numerical examples, the value of N is set to the total number of received samples in a communication session. The signal values $\mathrm{r}_m(nT - \varsigma(m, \theta))$ in (3) are recovered by interpolation of the digital signal $\mathrm{r}_m(i)$ from the mth hydrophone at time instants $t = nT - \varsigma(m, \theta)$, where $T = 1/f_s$; for this purpose, we use the linear interpolation.

The delays are different for each direction θ, computed as

$$\varsigma(m, \theta) = \frac{\mathrm{D}(m)\sin(\theta)}{c}, \tag{4}$$

where $\mathrm{D}(m)$ is the distance between the first ($m = 1$) and the mth hydrophone, and the sound speed $c = 1500$ m/s. The spatial signal power $\tilde{\mathrm{P}}(\theta)$ is computed according to

$$\tilde{\mathrm{P}}(\theta) = \left[\sum_{m=1}^{M}\sum_{n=1}^{M}[\mathbf{R}^{-1}(\theta)]_{m,n}\right]^{-1}. \tag{5}$$

In our numerical results, a direction grid in the interval $\theta \in [-25°, 25°]$ with a step of 0.1° is used.

3.1.2. FD Beamformer

The beamforming weights for a direction θ are computed as

$$\tilde{\mathrm{w}}(\theta) = \tilde{\mathrm{P}}(\theta)\left[\sum_{n=1}^{M}[\mathbf{R}^{-1}(\theta)]_{1,n}, \ldots, \sum_{n=1}^{M}[\mathbf{R}^{-1}(\theta)]_{M,n}\right]^T. \tag{6}$$

The static DOA $\hat{\theta}$ is estimated from the peak of the power $\tilde{\mathrm{P}}(\theta)$ for an entire communication session. The received signal for a DOA $\hat{\theta}$ is then computed as

$$\mathrm{r}(i, \hat{\theta}) = \left[\mathbf{X}^T(\hat{\theta})\tilde{\mathrm{w}}(\hat{\theta})\right]_i. \tag{7}$$

3.1.3. FD Complexity

The FD beamforming technique uses interpolation and processes each direction separately, making this spatial filter complicated [8].

The DOA estimator requires the interpolation in (3), computation of the covariance matrix in (2), and the power computation in (5); complexity of the other processing can be ignored. The complexity of these three steps is given by $4N_\theta M f_s$, $4N_\theta M^2 f_s$, and $4N_\theta M^2$ multiply-accumulate operations (MACs) per s, respectively; M is the number of antenna elements, and N_θ is the number of directions in the direction grid. In the beamformer, the weight computation in (6) needs to be performed; the other operations require significantly lower complexity. This step requires $(4M^2 f_s + 2M f_s)$ MACs per s. For example, with $M = 14$, $N_\theta = 501$, and $f_s = 12288$ Hz, i.e., with parameters used in the receiver in Section 2.2, the total complexity of the spatial filter is 5.2×10^9 MACs per s.

3.2. TFT-CSDM beamforming

Spatial filter using the TFT-CSDM beamforming first divides the continuous time domain received signals into L frames, and then transfers these time domain frames into frequency domain for DOA estimation and beamforming. Finally, the weighted frequency domain signal is transformed back into time domain. The pseudo code for the TFT-CSDM beamforming is shown in Algorithm 2.

Algorithm 2 TFT-CSDM beamforming

Require: hydrophone positions, received signals $\mathbf{r}(i) = [\mathrm{r}_1(i), \ldots, \mathrm{r}_M(i)]^T$, frequency bin width $\Delta\omega$;
Ensure: frequency bandwidth F, frequency bin number $K = 2\pi F/\Delta\omega$, interested direction θ;

procedure
  for $k = 0, 1, \ldots, K-1$ **do**
    compute frequency domain snapshot $\mathbf{z}(i_l; k) = \sum_{n=0}^{I_L-1} \mathbf{r}(i_l + n) e^{-j\omega_k n/f_s}$
    compute CSDM $\mathbf{Y}(i_l; k) = \frac{1}{L} \sum_{l=1}^{L} \mathbf{z}(i_l + (l-1)I_L; k)\mathbf{z}^*(i_l + (l-1)I_L; k) + \kappa \mathbf{I}_M$
    compute steering vector $\mathbf{v}(\theta, k) = \left[1, \ldots, e^{-j\omega_k \frac{\mathrm{D}(m)\sin(\theta)}{c}}, \ldots, e^{-j\omega_k \frac{\mathrm{D}(M)\sin(\theta)}{c}}\right]$
    compute power $\mathrm{P}_k(i_l; \theta) = \left[\mathbf{v}^H(\theta, k)\mathbf{Y}^{-1}(i_l; k)\mathbf{v}(\theta, k)\right]^{-1}$
  end for
  compute average power $\tilde{\mathrm{P}}(\theta) = \frac{1}{L} \sum_{l=1}^{L} \sum_{k=0}^{K-1} \mathrm{P}_k(i_l; \theta)$
  find maximum power $P_{\max} = \max_m P_m \to \hat{\theta}$ ▷ DOA estimation
  for $k = 0, 1, \ldots, K-1$ **do**
    compute weight factor $\bar{\mathbf{w}}_l(\hat{\theta}, k) = \mathbf{Y}^{-1}(i_l; k)\mathbf{v}(\hat{\theta}, k)\mathrm{P}_k(i_l; \hat{\theta})$
    smooth weight factor $\mathbf{w}_l(\hat{\theta}, k) \leftarrow \lambda \mathbf{w}_{l-1}(\hat{\theta}, k) + (1-\lambda)\bar{\mathbf{w}}_l(\hat{\theta}, k)$
    beamformed signal $\mathrm{r}(i, \hat{\theta}) = \sum_{k=0}^{K-1} \mathbf{w}_l^*(\hat{\theta}, k)\mathbf{z}(i_l; k) e^{j\omega_k n/f_s}$ ▷ beamformed signal
  end for
end procedure

3.2.1. TFT-CSDM DOA estimator

The DOA estimator computes the spatial power distribution of the received signal by processing the hydrophone signals $\mathrm{r}_1(i)$ to $\mathrm{r}_M(i)$. The ith time domain snapshot of the received signals is described as an $M \times 1$ vector $\mathbf{r}(i) = [\mathrm{r}_1(i), \ldots, \mathrm{r}_M(i)]^T$. The snapshots are divided into L frames of I_L snapshots each. The $M \times 1$ frequency domain snapshot at frequency ω_k for a frame starting at time instant i_l is given by

$$\mathbf{z}(i_l; k) = \sum_{n=0}^{I_L-1} \mathbf{r}(i_l + n) e^{-j\omega_k n/f_s}, \tag{8}$$

where $k = 0, 1, \ldots, K-1$, $K = 2\pi F/\Delta\omega$, F is the bandwidth of interest, $\omega_k = \omega_0 + k\Delta\omega$, $\Delta\omega = 2\pi\Delta f$, and ω_0 is the lowest frequency of interest ($\omega_0 = 2\pi(f_c - F/2)$ here). For a frame starting at time instant i_l, for every frequency ω_k, the $M \times M$ cross spectral density matrix (CSDM) is computed as [28]:

$$\mathbf{Y}(i_l; k) = \frac{1}{L} \sum_{l=1}^{L} \mathbf{z}(i_l + (l-1)I_L; k)\mathbf{z}^*(i_l + (l-1)I_L; k) + \kappa \mathbf{I}_M, \tag{9}$$

where $(\cdot)^*$ denotes the conjugate transpose, l is the frame index, and κ is a loading factor which is a small positive number related to the noise level. In the experiments, the loading factor κ was set to a small value to prevent numerical instability when inverting the matrix $\mathbf{Y}(i_l; k)$ (see below). More specifically, it was set to at most 10^{-8} of $(1/M)\mathrm{trace}\{\mathbf{Y}(i_f; k)\}$, where trace$\{\cdot\}$ is the matrix trace. The loading factor κ can be optimized to achieve an improved detection performance [29], while such optimization is not detailed here. The matrix $\mathbf{Y}(i_l; k)$ is used for obtaining the spatial power at every direction θ.

For beamforming, various algorithms have been presented in literature, e.g., conventional classic beamforming [30, 31, 32], minimum norm beamforming (MINNORM), Multiple Signal Classification Algorithm (MUSIC), root-MUSIC, Estimation of signal parameters via rotation invariance techniques (ESPRIT), minimum variance distortionless response algorithm (MVDR), etc. [33, 34, 35]. The classic beamforming algorithm does not provide high resolution [36], while the MINNORM, MUSIC, root-MUSIC, and ESPRIT algorithms [37] are able to provide high resolution on the DOA estimation. However, these high resolution algorithms are often based on the computation of inverse QR-based decomposition, which introduces complexity. The matrix inversion unit of the decomposition only works for a fixed set of matrix [38], which limits the implementation of these high resolution algorithms in UWA communications with long data sets. Thus here we choose an algorithm without using the QR-based decomposition, i.e., MVDR algorithm [39, 40] to compute the spatial power.

For a frequency ω_k, the steering vector is given by

$$\mathbf{v}(\theta, k) = \Big[1, \ldots, e^{-j\omega_k \frac{\mathrm{D}(m)\sin(\theta)}{c}}, \ldots, e^{-j\omega_k \frac{\mathrm{D}(M)\sin(\theta)}{c}}\Big]. \tag{10}$$

The power at frequency ω_k from a direction θ is given by:

$$\mathrm{P}_k(i_l;\theta) = \left[\mathbf{v}^H(\theta,k)\mathbf{Y}^{-1}(i_l;k)\mathbf{v}(\theta,k)\right]^{-1}, \tag{11}$$

and the total power for all frequencies of interest is given by

$$\mathrm{P}(i_l;\theta) = \sum_{k=0}^{K-1} \mathrm{P}_k(i_l;\theta). \tag{12}$$

The average power over L frames is given by

$$\tilde{\mathrm{P}}(\theta) = \frac{1}{L}\sum_{l=1}^{L} \mathrm{P}(i_l;\theta). \tag{13}$$

3.2.2. TFT-CSDM Beamformer

In this case, the DOA $\hat{\theta}$ is chosen from the peak of the $\tilde{\mathrm{P}}(\theta)$ for an entire communication session. For a chosen DOA $\hat{\theta}$, to cancel the interference arriving from other directions, the beamformer weight vector $\bar{\mathbf{w}}_l(\hat{\theta}, k)$ in the lth frame is calculated as [39]:

$$\bar{\mathbf{w}}_l(\hat{\theta}, k) = \mathbf{Y}^{-1}(i_l;k)\mathbf{v}(\hat{\theta},k)\mathrm{P}_k(i_l;\hat{\theta}). \tag{14}$$

The weight vector is then smoothed in time:

$$\mathbf{w}_l(\hat{\theta}, k) \leftarrow \lambda \mathbf{w}_{l-1}(\hat{\theta}, k) + (1-\lambda)\bar{\mathbf{w}}_l(\hat{\theta}, k), \tag{15}$$

where $0 \le \lambda < 1$ is a forgetting factor, and $\mathbf{w}_0(\hat{\theta}, k) = \bar{\mathbf{w}}_1(\hat{\theta}, k)$. The directional signal is then computed as:

$$\mathrm{r}(i, \hat{\theta}) = \sum_{k=0}^{K-1} \mathbf{w}_l^*(\hat{\theta}, k)\mathbf{z}(i_l;k)e^{j\omega_k n/f_s}, \tag{16}$$

where $i = i_l + (l-1)I_L + n$.

3.2.3. TFT-CSDM Complexity

For the DOA estimation, the spatial filter requires the time-frequency transform in (8), computation of the CSDM in (9), and the power computation in (11); complexity of the other processing can be ignored. The complexity of these three steps is given by $2KMf_s$, $4Kf_sM^2/I_L$, and $4(KM^3 + KN_\theta M^2)$ MACs per s, respectively; M is the number of antenna elements, K is the number of frequencies in the transform, and N_θ is the number of directions in the direction grid. In a beamformer, the frequency-time transform in (16) needs to be performed; the other operations require significantly lower complexity. This step requires $(4KMf_s/I_L + 4Kf_s)$ MACs per s. For example, with $M = 14$, $K = 16$, $f_s/I_L = 1$, $N_\theta = 501$, and $f_s = 12288$ Hz, i.e., with parameters used in the receiver in Section 2.2, the total complexity of the spatial filter is 1.3×10^7 MACs per s.

3.3. Proposed TFT-CPSD beamforming

When the gradient of sound is significant along the array aperture, the wave front is not spherical and beamforming should be replaced with a mode filtering, otherwise energy leakage cannot be avoided. The continuing processing of signal block (frame) with different delays cannot be done by blocks and FFT, because of the tail with delayed signals. Thus, convolution methods, overlap-save or overlap-add methods are needed [41, 42]. Different from the existing TFT-CSDM beamforming, the TFT-CPSD beamforming first applies the overlap-save method for a frame length I_L, then computes the cross power spectral density (CPSD) instead of CSDM for each segment to obtain spatial power, uses window (Hamming window here) to filter data for each frame, and smooths the weight vector using a moving average filter on neighbour frames instead of that from the past frames initiated from the first frame as shown in (15). The pseudo code for the TFT-CPSD beamforming is concluded in Algorithm 3.

Algorithm 3 TFT-CPSD beamforming

Require: hydrophone positions, received signals $\mathbf{r}(i) = [\mathrm{r}_1(i), \ldots, \mathrm{r}_M(i)]^T$, frequency bin width $\Delta\omega$;
Ensure: frequency bandwidth F, frequency bin number $K = 2\pi F/\Delta\omega$, interested direction θ;

procedure
  reconstruct each data frame $\mathbf{r}(i_l)$ with the overlap-save method
  for $k = 0, 1, \ldots, K-1$ **do**
    compute cross-correlation sequence $\tilde{\mathbf{R}}(i_l; m) = E\{\mathbf{r}(i_l + n + m)\mathbf{r}(i_l + n)^*\}$
    compute CPSD $\tilde{\mathbf{C}}(i_l, k) = \sum_{m=-I_L}^{I_L} \tilde{\mathbf{R}}(i_l; m)e^{-j\omega_k m}$
    compute steering vector $\mathbf{v}(\theta, k) = \left[1, \ldots, e^{-j\omega_k \frac{\mathrm{D}(m)\sin(\theta)}{c}}, \ldots, e^{-j\omega_k \frac{\mathrm{D}(M)\sin(\theta)}{c}}\right]$
    compute power $\mathrm{P}_k(i_l; \theta) = \left[\mathbf{v}^*(\theta, k)\tilde{\mathbf{C}}(i_l, k)\mathbf{v}(\theta, k)\right]^{-1}$
  end for
  compute average power $\tilde{\mathrm{P}}(\theta) = \frac{1}{L}\sum_{l=1}^{L}\sum_{k=0}^{K-1} \mathrm{P}_k(i_l; \theta)$
  find maximum power $P_{\max} = \max_m P_m \rightarrow \hat{\theta}$ ▷ DOA estimation
  for $k = 0, 1, \ldots, K-1$ **do**
    compute weight factor $\bar{\mathbf{w}}_l(\hat{\theta}, k) = \tilde{\mathbf{C}}^{-1}(i_l; k)\mathbf{v}(\hat{\theta}, k)\mathrm{P}_k(i_l; \hat{\theta})$
    smooth weight factor $\mathbf{w}_l(\hat{\theta}, k) \leftarrow \frac{\bar{\mathbf{w}}_{l-l_d}(\hat{\theta},k)+\cdots+\bar{\mathbf{w}}_l(\hat{\theta},k)+\cdots+\bar{\mathbf{w}}_{l+l_d}(\hat{\theta},k)}{2l_d+1}$
    compute frequency domain snapshot $\mathbf{z}(i_l; k) = \sum_{n=0}^{I_L-1} \mathbf{r}(i_l + n)e^{-j\omega_k n/f_s}$
    beamformed signal $\mathrm{r}(i, \hat{\theta}) = \sum_{k=0}^{K-1} \mathbf{w}_l^*(\hat{\theta}, k)\mathbf{z}(i_l; k)e^{j\omega_k n/f_s}$ ▷ beamformed signal
  end for
end procedure

3.3.1. TFT-CPSD DOA estimator

The DOA estimator computes the spatial power distribution of the received signal by processing the hydrophone signals $\mathrm{r}_1(i)$ to $\mathrm{r}_M(i)$. The ith time domain snapshot of the received signals is described as an $M \times 1$ vector $\mathbf{r}(i) = [\mathrm{r}_1(i), \ldots, \mathrm{r}_M(i)]^T$.

The snapshots are then divided into L frames of I_L snapshots each. Different from the TFT-CSDM beamforming, here the frame is overlapped with its previous frame. Each frame has a length of I_L and has an overlap length I_{Lo} with its previous frame. Here we set the overlap length I_{Lo} as half of I_L, and will investigate the length for each frame with the experimental data presented in Section 5.1.1. For each frame, we use a Hamming window of length H_{win} to filter the data segments of that window length. For a frame starting at time instant i_l, for every frequency of interest ω_k, the CPSD is the distribution of power per unit frequency defined as [43, 44]

$$\tilde{\mathbf{C}}(i_l, k) = \sum_{m=-I_L}^{I_L} \tilde{\mathbf{R}}(i_l; m)e^{-j\omega_k m}. \tag{17}$$

The frequency of interest ω_k is chosen from a bin vector with a bin width of $\Delta\mathrm{F} = F/K$, where K is the number of bins and F is the bandwidth. For each bin, we integrate the wideband across the frequency bin width $\Delta\mathrm{F}$ assuming that the variation in a bin can be omitted.

The cross-correlation sequence $\tilde{\mathbf{R}}(i_l; m)$ is defined as

$$\tilde{\mathbf{R}}(i_l; m) = E\{\mathbf{r}(i_l + n + m)\mathbf{r}(i_l + n)^*\}, \tag{18}$$

where $\mathbf{r}(i_l+n)$ is the snapshots in the lth frame, $-I_L < n < I_L$ and $-I_L < m < I_L$ for a single frame, and $E\{\cdot\}$ is the expected value operator. In practice, it can be achieved by computing

$$\tilde{\mathbf{R}}(i_l;m) = \begin{cases} \sum_{n=0}^{N-m-1} \mathbf{r}(i_l+n+m)\mathbf{r}^*(i_l+n), & (m \geq 0) \\ \tilde{\mathbf{R}}^*(i_l;-m), & (m < 0) \end{cases} \tag{19}$$

with normalization to produce an accurate estimate.

The CPSD $\tilde{\mathbf{C}}(i_l,k)$ is used for obtaining the spatial power at every direction θ using the MVDR algorithm [39, 40]. For a frequency ω_k, the steering vector is given by (10). The power at frequency ω_k from a direction θ is given by:

$$\mathrm{P}_k(i_l;\theta) = \left[\mathbf{v}^*(\theta,k)\tilde{\mathbf{C}}(i_l,k)\mathbf{v}(\theta,k)\right]^{-1}. \tag{20}$$

and the total power for all frequencies of interest is given by

$$\mathrm{P}(i_l;\theta) = \sum_{k=0}^{K-1} \mathrm{P}_k(i_l;\theta). \tag{21}$$

The average power over L frames is given by

$$\tilde{\mathrm{P}}(\theta) = \frac{1}{L}\sum_{l=1}^{L} \mathrm{P}(i_l;\theta). \tag{22}$$

3.3.2. TFT-CPSD Beamformer

In this case, the DOA $\hat{\theta}$ is also chosen from the peak of the $\tilde{\mathrm{P}}(\theta)$ for the entire session. For a chosen DOA $\hat{\theta}$, to cancel the interference arriving from other directions, the beamformer weight vector $\bar{\mathbf{w}}_l(\hat{\theta},k)$ in the lth frame is calculated as [39]:

$$\bar{\mathbf{w}}_l(\hat{\theta},k) = \tilde{\mathbf{C}}^{-1}(i_l;k)\mathbf{v}(\hat{\theta},k)\mathrm{P}_k(i_l;\hat{\theta}). \tag{23}$$

Due to ocean dynamics resulting in fluctuations of DOA during the communication session, the DOA associated weights may change significantly from the beginning. Instead of using iterative smooth from the past frames as shown in (15), we introduce an average smooth, in which the weight vector is smoothed using a moving average filter. The filter uses a number of data points $l_d = \hat{\lambda}L/2$ for calculating the smoothed value. The parameter $\hat{\lambda}/2$ is in the range (0,1) denoting a fraction of the total number of data points. The weight vector is then smoothed as:

$$\mathbf{w}_l(\hat{\theta},k) \leftarrow \frac{\bar{\mathbf{w}}_{l-l_d}(\hat{\theta},k) + \cdots + \bar{\mathbf{w}}_l(\hat{\theta},k) + \cdots + \bar{\mathbf{w}}_{l+l_d}(\hat{\theta},k)}{2l_d+1}, \tag{24}$$

where $\mathbf{w}_1(\hat{\theta},k) = \bar{\mathbf{w}}_1(\hat{\theta},k)$, and $\mathbf{w}_2(\hat{\theta},k) = \frac{\bar{\mathbf{w}}_1(\hat{\theta},k)+\bar{\mathbf{w}}_2(\hat{\theta},k)}{2}$, etc. The directional signal is then computed as:

$$\mathrm{r}(i,\hat{\theta}) = \sum_{k=0}^{K-1} \mathbf{w}_l^*(\hat{\theta},k)\mathbf{z}(i_l;k)e^{j\omega_k n/f_s}, \tag{25}$$

where $i = i_l + (l-1)I_L + n$. While adding these directional signal snapshots together, we overlap the extra data length Lo to reduce the tail effect and energy leakage.

3.3.3. TFT-CPSD Complexity

For the DOA estimation, the spatial filter requires the cross-correlation in (18), the computation of CPSD in (17), and the power computation in (20); complexity of the other processing can be ignored. The complexity of the cross-correlation is computed from the integration of the number of non-zeros multiplications. The complexity of these three steps is given by $4M^2 f_s(H_{\mathrm{win}}+1)/2$, $2KMf_s$, and $4(KM^3 + KN_\theta M^2)$ MACs per s, respectively. In a beamformer, the frequency-time transform in (25) needs to be performed; the other operations require significantly lower complexity. This step requires $(4KMf_s/I_L + 4Kf_s)$ MACs per s. For example, with $M = 14$, $K = 16$, $H_{\mathrm{win}} = 16$, $N_\theta = 501$, and $f_s = 12288$ Hz, i.e., with parameters used in the receiver in Section 2.2, the total complexity of the spatial filter is 9.5×10^7 MACs per s.

4. Accuracy of DOA estimation

To compare the accuracy of DOA estimator and detection capability of using the three beamforming techniques, we use the data recorded in the sea trial session F1-1 at a transmitter to receive VLA distance of 30 km (detailed in Section 5).

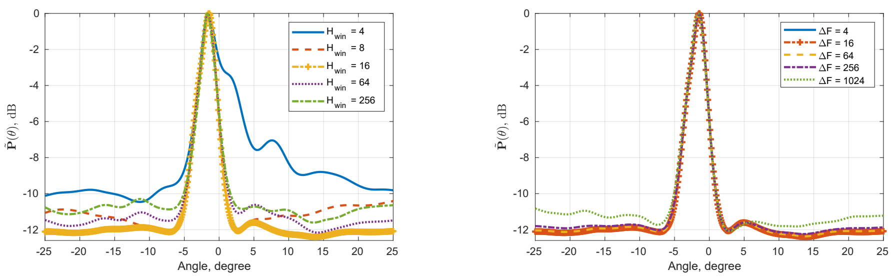

(a) frequency bin $\Delta\mathrm{F} = 16$ Hz, varying window length H_{win}.

(b) $H_{\mathrm{win}} = 16$, varying frequency bin $\Delta\mathrm{F}$; $\Delta\mathrm{F} = 4$ is invisible.

Figure 2: Comparisons of average spatial signal power $\tilde{\mathrm{P}}(\theta)$ estimated from the DOA estimator using the proposed TFT-CPSD beamforming with different window length and frequency bins in the sea trial session at a distance of 30 km. (a) varying window length; (b) varying frequency bin.

4.1. Parameter justification of TFT-CPSD

We first justify the values of window length and frequency bin of the proposed TFT-CPSD algorithm. Fig. 2 shows comparison results of average spatial signal power $\tilde{\mathrm{P}}(\theta)$ of the DOA estimator at various window lengths and frequency bins. Fig. 2(a) shows that when the frequency bin $\Delta\mathrm{F} = 16$ Hz, the DOA estimator shows the best accuracy as the window length $H_{\mathrm{win}} = 16$ samples; and Fig. 2(b) shows that when the window length $H_{\mathrm{win}} = 16$ samples, the accuracy of DOA estimator increases as the frequency bin $\Delta\mathrm{F}$ decreases, while it is almost unchanged as $\Delta\mathrm{F} \leq 64$ Hz.

Thus we choose $H_{\mathrm{win}} = 16$ and $\Delta\mathrm{F} = 64$ Hz for further processing. When processing the received signals in the spatial filter, $K = 1024/64 = 16$ frequencies are processed in the bandwidth of interest $F = 1024$ Hz, and the lowest frequency of interest $f_0 = \omega_0/(2\pi) = 2560$ Hz. The frame length I_f is considered to be one OFDM symbol length here, and the loading factor $\kappa = 10^{-3}$. The DOAs θ for DOA estimation are computed in $[-25°, 25°]$ with a DOA step of $0.1°$.

4.2. Comparison of DOA estimators

Fig. 3 shows comparison results of average spatial signal power $\tilde{\mathrm{P}}(\theta)$ estimated from the DOA estimator using the three beamforming techniques at different SNRs, i.e., [-15, -5, 5, 14] dB, by adding measured ambient noise to received signal for each hydrophone channel. The proposed DOA estimator using the proposed TFT-CPSD beamforming outperforms that using the TFT-CSDM beamforming in accuracy, while it is inferior to that of using the FD beamforming, obvious at high SNRs. However, at low SNRs, the FD beamforming shows significant beamforming leakage of the target signal into the interference at multiple angles, which makes the accuracy of it worse and makes the DOA detection difficult.

The computational complexity of the DOA estimator using the three beamforming techniques are compared in TABLE 1. The complexity of DOA estimator using the proposed TFT-CPSD beamforming is significantly lower than that of using the FD beamforming, while it is not much higher than that of using the TFT-CSDM beamforming.

Table 1: Complexity of DOA estimator with different beamforming

Beamforming	**Complexity (10^6 MAC/s)**
no beamforming	0
FD	5200
TFT-CSDM	13
TFT-CPSD (proposed)	95

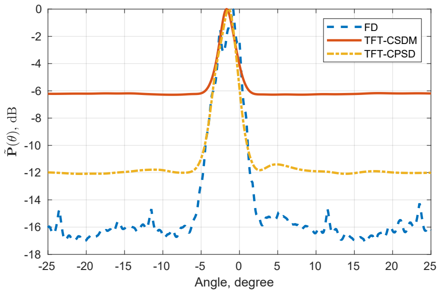

(a) SNR = 14 dB

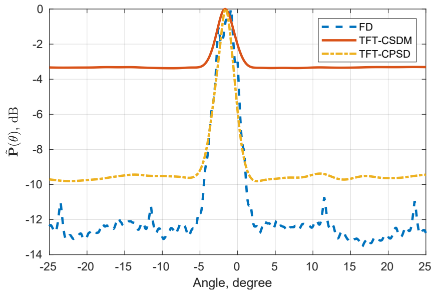

(b) SNR = 5 dB

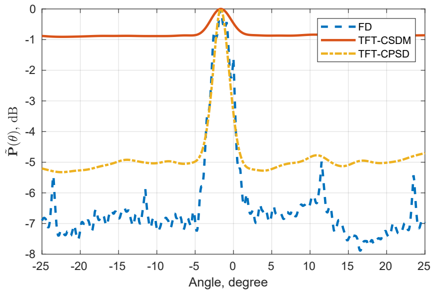

(c) SNR = -5 dB

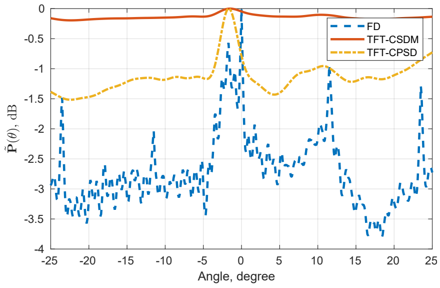

(d) SNR = -15 dB

Figure 3: Comparisons of average spatial signal power $\widetilde{\mathrm{P}}(\theta)$ estimated from the DOA estimator using the FD beamforming, the TFT-CSDM beamforming, and the proposed TFT-CPSD beamforming in the sea trial session F1-1 at different SNRs. (a) 14 dB. (b) 5 dB. (c) -5 dB. (d) -15 dB.

5. Receiver performance

In this section, we compare the receiver with DOA estimator using different beamforming techniques. To demonstrate the effectiveness of the proposed TFT-CPSD beamforming used in the receiver, comparisons are performed with the transmission of guard-free OFDM signals with superimposed data and pilot [23]. These comparisons use data from two sessions in the northwest Pacific Ocean sea trial, i.e.,

- session F1-1: transmitter to receiver distance of 30 km;
- session F-3: transmitter to receiver distance of 50 km.

In both sessions, the depth of the transmitter was 250 m, and the depth of the first receive VLA hydrophone was 420 m (Fig. 4). In the receive VLA, the distances from the mth hydrophones in turn to the first (top) hydrophone are [0 0.6 1.2 1.8 2.4 3.0 3.6 3.9 4.8 5.4 6.0 6.6 7.8 8.1] m. The sound-speed profile (SSP) measured in the sea trial area is shown in Fig. 5, showing the gradient of sound. The sea

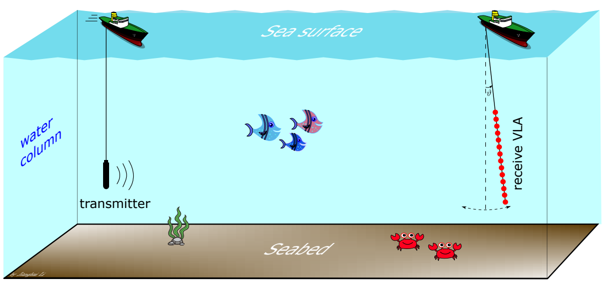

Figure 4: Sea trial scenario in the northwest Pacific Ocean. The depth of the transmitter was 250 m, and the depth of the first receive VLA hydrophone was 420 m. The length of the receive VLA of hydrophones is 8.1 m. The receive VLA oscillation can be resulted from the ocean dynamics. Underwater ambient noise in the communication channel can be radiated from surface wave agitation, shipping, marine animals, turbulence, etc. [45, 46, 47, 48, 49, 50, 51, 52].

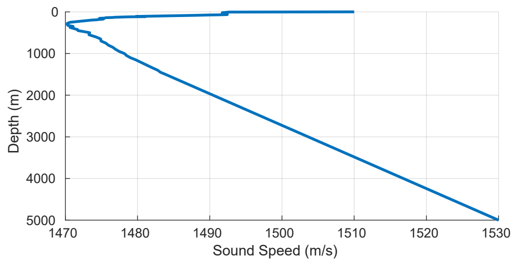

Figure 5: Sound speed profiles (SSP) measured in the sea trial area (northwest Pacific Ocean), and used in the simulation (Section 6).

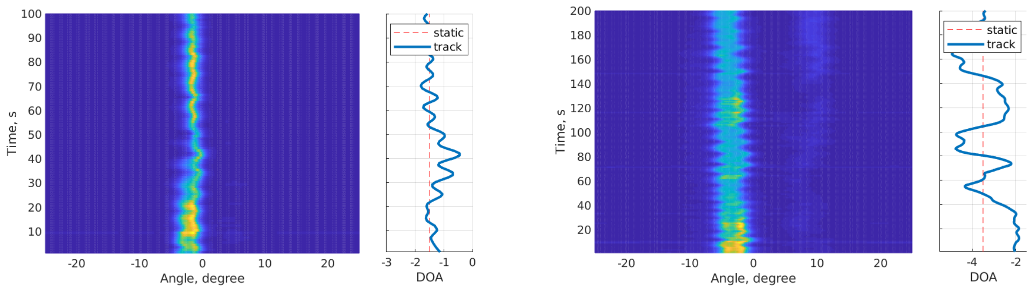

(a) F1-1 session, 30 km, static DOA = -1.4°.

(b) F-3 session, 50 km, static DOA = -3.5°.

Figure 6: DOA fluctuation in the sea trial. (a) F1-1 session, 30 km; (b) F-3 session, 50 km. Left: estimated spatial signal power; right: angle of spatial power peak for the entire session (red dashed line), and angle of spatial power peak for each data frame (blue solid line).

depth is about 5 km, and the minimum sound speed is at a depth of about 300 m. In the two sea trial sessions, communication signals are transmitted in the frequency band 2560-3584 Hz.

5.1. *Session F1−1*

In the F1−1 session, the transmitter was towed by a vessel moving towards the receiver at a high speed of 8 m/s, and the distance between them varied from 30 to 29 km. In this session, 100 guard-free OFDM symbols were transmitted. Fig. 6(a) left side shows the spatial power distribution. It can be seen that an outstanding cluster is identified as the one with DOA around $\hat{\theta} = -1.4°$. Fig. 6(a) right side shows the time-varying DOA detected for each frame (blue solid line) and a static DOA $\hat{\theta} = -1.4°$ chosen from the average spatial power peak for the entire communication session (red dashed line). The time-varying DOA across the static DOA possesses a maximum variance of 1.5° from ocean dynamics. The static angle $\hat{\theta} = -1.4°$ is used to produce a directional signal using the three beamforming techniques.

Fig. 7(a) shows the time-varying SNR at the first receive VLA hydrophone in the F1-1 session, which is the result of received signal energy divided by recorded noise energy in frames. The SNR varies between 7 dB and 18.5 dB, and on average is 14 dB, indicating complex noise levels in the communication channel. Fig. 8(a) shows fluctuations of the channel impulse response over the F1-1 session at the first hydrophone, revealing a single outstanding propagation path of the transmitted signal in the channel.

5.1.1. *Frame length investigation*

Underwater acoustic channel is often characterized as fast-varying both in time domain and frequency domain. Time-variation of DOA and Doppler can be significant from one frame to the other. The continuous processing of signal frames with different delays introduces energy leakage inevitably because of the tail of delayed signals. To reduce such leakage, we investigate the optimal frame length adapting to the specific channel for the process of continuous signal in the receiver. Here we investigate the frame length in the receiver based on the data collected from the session F1-1.

In the investigation, the TFT-CPSD beamforming is implemented in the receiver, and the frame length is set to 1 second (s), 1/3 s, 1/6 s, 1/12 s, and 1/24 s, respectively. Fig. 9 shows the bit error rate (BER) performance of the receiver as different length frames are processed. It shows that when the

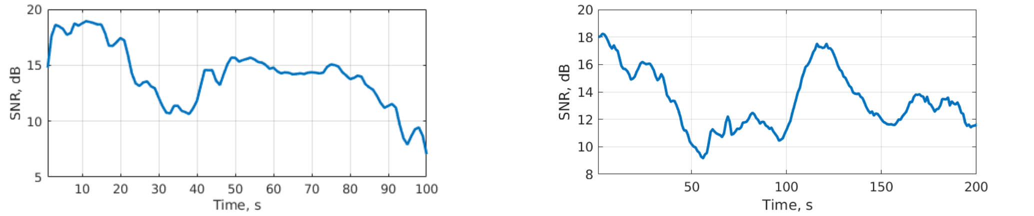

(a) F1-1 session, 30 km, average SNR = 14 dB. (b) F-3 session, 50 km, average SNR = 14 dB.

Figure 7: Time-varying SNR at the first (top) hydrophone channel in the sea trial. (a) F1-1 session, 30 km; (b) F-3 session, 50 km.

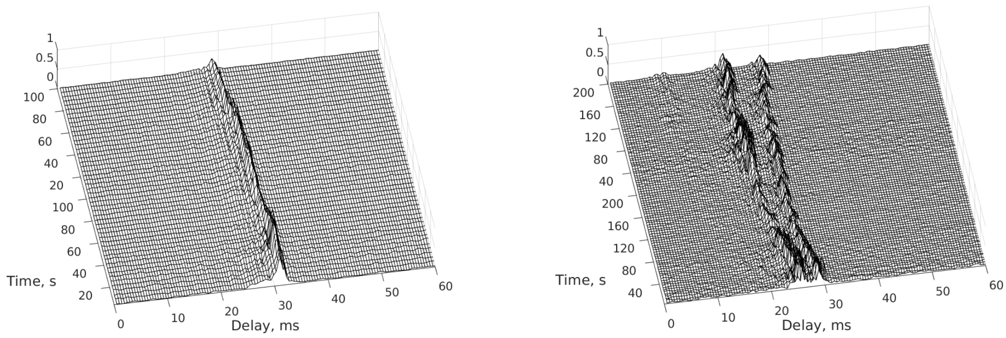

(a) F1-1 session, 30 km. (b) F-3 session, 50 km.

Figure 8: Fluctuations of the channel impulse response at the first hydrophone in the two communication sessions. (a) F1-1 session; (b) F-3 session.

frame length is set to 1/6 s, the receiver shows the best performance at SNR higher than 0 dB. It also shows that the receiver is sensitive to the frame length at high SNR, while it is insensitive at low SNR.

5.1.2. BER performance comparison

The BER performances of the receiver using the three beamforming techniques based DOA estimator are now compared. To show the performance of the receiver at different SNR, we add noise to the received signals separately. Signals with lower SNR are produced by adding measured ambient noise from each hydrophone to the received signal with SNR of 14 dB (Fig. 7(a)). Note that the ambient noise varies in bathymetry and the depth/position of hydrophones, resulting in specific relationship/correlations among these channel noises recorded by the 14 hydrophones (see details in Appendix A). Fig. 10 presents the BER performance of the receiver applied to the sea trial data recorded in the F1-1 session at spectral efficiencies of (a) 1 bps/Hz and (b) 0.5 bps/Hz; the convolutional code represented by polynomial in octal [3 7], being rate-1/2 code [27] is used.

Results presented in Fig. 10 demonstrate that when the SNR increases from -14 dB to 14 dB, the receiver with all the three beamforming techniques show improved detection performance at both spectral efficiencies compared to that without using beamforming. The receiver using the proposed TFT-CPSD beamforming provides better performance through the entire range of SNR than the FD beamforming and the TFT-CSDM beamforming, with only slightly comparable at high SNR ($>$ 9 dB) to the FD beamforming at spectral efficiency of 1 bps/Hz. At a lower spectral efficiency (1/2 bps/Hz), the receiver using the TFT-CPSD beamforming technique outperforms both the FD beamforming and TFT-CSDM beamforming, and achieves error-free transmission at SNR $\geq$ -2 dB, showing better detection performance than that of using the other two beamforming techniques. The TFT-CPSD performs better than the FD beamforming because of its reduced energy leakage between overlapped segments. The TFT-CPSD performs better than the TFT-CSDM beamforming because of its fully considered energy of the received signals.

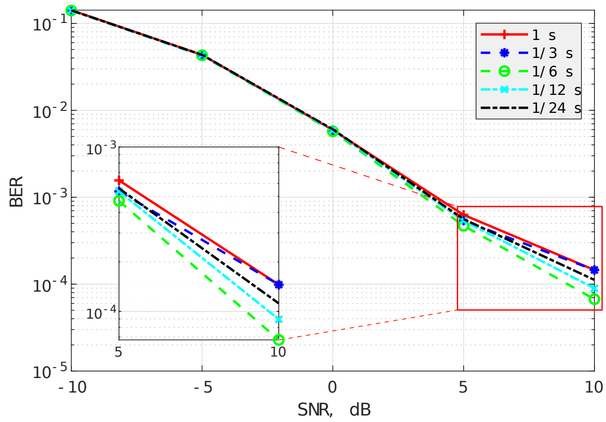

Figure 9: BER performance of the receiver with different signal frame length (1 s, 1/3 s, 1/6 s, 1/12 s, and 1/24 s). It shows the best performance as the frame length set to 1/6 second (s).

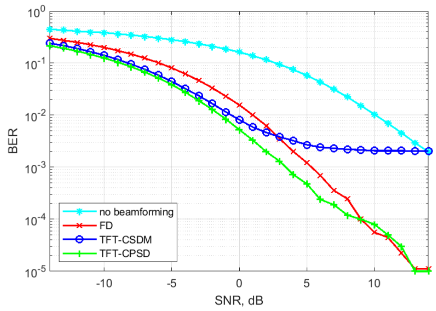

(a) 1 bps/Hz.

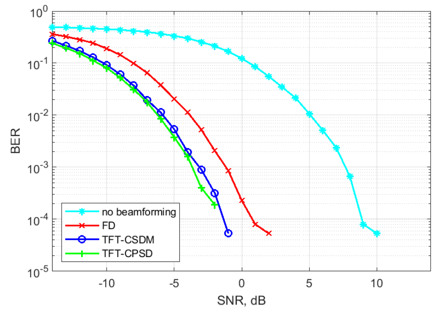

(b) 1/2 bps/Hz; error-free transmissions are not shown.

Figure 10: BER performance of the receiver without using beamforming and with the DOA estimator using the three beamforming techniques in the F1-1 session in the function of SNR at different spectral efficiencies. (a) 1 bps/Hz (1024 bits/s); (b) 1/2 bps/Hz (512 bits/s).

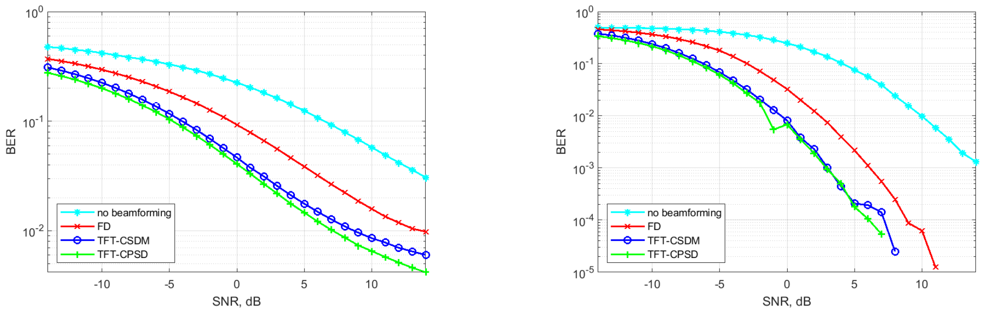

(a) 1 bps/Hz.

(b) 1/2 bps/Hz; error-free transmissions are not shown.

Figure 11: BER performance of the receiver without using beamforming and with the DOA estimator using the three beamforming techniques in the F-3 session in the function of SNR at different spectral efficiencies. (a) 1 bps/Hz (1024 bits/s); (b) 1/2 bps/Hz (512 bits/s).

5.1.3. Session F−3

In the F−3 session, the transmitter was towed by a vessel moving away from the receive VLA at a speed of 3 m/s, and the distance between them varied from 50 to 51 km. In this session, 200 guard-free OFDM symbols were transmitted. Fig. 6(b) left side shows the spatial power distribution. It can be seen that a mixed cluster, i.e., mixed by two separated sub-clusters from two time-varying arrival DOAs as observed, is identified as with DOA around $\hat{\theta} = -3.5°$. Due to the difficulty of separating the two sub-clusters as in such close angle case, we consider it as a single cluster to find the static DOA with the peak of average spatial signal power through the session (see [10] for technique of processing multiple DOA branches). Fig. 6(b) right side shows the time-varying DOA detected for each frame (blue solid line) and a static DOA for the entire communication session (red dashed line). The peak of time-varying DOA changes between the two sub-clusters through the session indicates comparable strength of the two path arrivals. The time-varying DOA across the static DOA possesses a maximum variation of 3.0°. The static DOA is used to produce a single directional signal.

Fig. 7(b) shows the time-varying SNR at the first receive VLA hydrophone in the F-3 session, varying between 9 dB and 18 dB, and on average is 14 dB. Fig. 8(b) shows fluctuations of the channel impulse response over the F-3 session at the first hydrophone, revealing two outstanding path arrivals from the channel. Rather than possessing an outstanding single channel path, this session possesses a more complicated propagation path arrivals from two outstanding channel paths, and sometimes they interact with each other. This makes the interpolation more difficult and less accurate.

Results presented in Fig. 11 demonstrate that the receiver using all the three beamforming techniques show improved detection performance at both spectral efficiencies with the SNR increasing from -14 dB to 14 dB compared to that without using beamforming technique. The receiver using the TFT-CPSD beamforming technique provides better performance than both the other beamforming techniques at both the spectral efficiencies of 1 bps/Hz and 1/2 bps/Hz. At a lower spectral efficiency (1/2 bps/Hz), the receiver using the TFT-CPSD beamforming technique achieves error-free transmission at SNR $\geq$ 7 dB, while the receiver using the other two beamforming techniques is unable to achieve error-free transmission at such SNR of 7 dB. This illustrates that the receiver with the FD beamforming and the TFT-CSDM beamforming is inferior to process such complex case of channel arrivals from multiple interacted directions than that of using the TFT-CPSD beamforming technique in UWA channels. The TFT-CPSD performs better than the other two beamforming techniques due to its reduced energy leakage with overlapped frames and its fully computed energy of received signals.

6. Verification of beamforming leakage

To verify the merit of no beamforming leakage from the proposed TFT-CPSD beamforming, we use the Waymark propagation model based simulation [24, 25, 26]. In the simulation, the transmitter is stationary at a depth of 300 m. The receive VLA is towed by an ocean surface platform, and has a periodic oscillation with a maximum oscillating angle of $\vartheta_M = 1.5°$, as shown in Fig. 4. When the oscillating angle $\vartheta(t) = 0°$, the depth of the first hydrophone is 300 m, and the distance between the transmitter and the receive VLA is 60 km. The SSP used in the simulation is shown in Fig. 5.

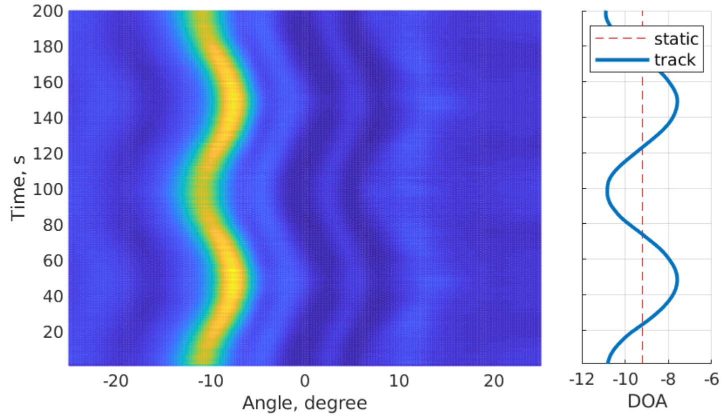

Figure 12: DOA fluctuation in the simulation. Transmitter to receive VLA distance is 60 km. Left: estimated spatial signal power; right: angle of spatial power peak for the entire session (red dashed line), and angle of spatial power peak for each data frame (blue solid line).

During the simulation, 200 guard-free OFDM symbols are continuously transmitted. The receive VLA oscillation is considered to be induced by the sea current/turbulence, consistent with that from the two sea trial sessions as shown in Fig. 6. The oscillating angle is given by

$$\vartheta(t) = -\vartheta_M \cos\left(\frac{2\pi t}{T_p}\right),\ t \in [0, T-1], \tag{26}$$

where $T_p = 100$ s is the period of the VLA oscillation, and $T = 200$ s the duration of the communication session, ignoring propagation time in the channel. Note that when the angle is on the left hand of the middle dashed vertical line (see Fig. 4), the $\vartheta(t)$ is set as a negative value; and vice versa.

Fig. 12 left side shows spatial power distribution in the simulation. It can be seen that an outstanding cluster is identified as the one with DOA around $\hat{\theta} = -9.2°$. Fig. 12 right side shows the time-varying DOA crossing the static DOA $\hat{\theta} = -9.2°$ computed from the average spatial signal power for the entire communication session.

Fig. 13 shows comparison results of average spatial signal power $\tilde{\mathrm{P}}(\theta)$ estimated from the DOA estimator using the three beamforming techniques with data from the Waymark model simulation without adding channel noise. The DOA estimator using the proposed TFT-CPSD beamforming outperforms that of using the TFT-CSDM beamforming in accuracy, while it is comparable to that using the FD beamforming. In this case of without adding channel noise, there are still multiple extra power peaks (black circles in Fig. 13) from the result of FD beamforming, which is the same as that with the sea trial data shown in Fig. 3. The result indicates that these peaks are from beamforming leakage associated with the FD beamforming rather than from the underwater ambient. Such leakage of the target signal into the interference at multiple angles is interpreted from the time domain interpolation, and makes the DOA detection difficult, especially at low SNR. The TFT-CPSD beamforming does not have such beamforming leakage problem while provides high detection accuracy.

7. Conclusions and discussion

In this paper, we exploit the capability of three beamforming techniques, including a proposed low complexity TFT-CPSD (time-frequency-time with cross power spectral density) beamforming, in time-varying underwater acoustic communication channels, for improving the accuracy of DOA estimation and the detection performance of a receive system. The investigated receiver is designed for an underwater acoustic communication system with the transmission of guard-free OFDM signals with superimposed pilot symbols. Sea trial results demonstrate that the DOA estimator using the proposed TFT-CPSD beamforming possesses higher accuracy than that of using an existing TFT-CSDM beamforming and lower complexity than that of using interpolation based FD beamforming. The receiver using the TFT-CPSD beamforming based DOA estimator outperforms that of using the FD beamforming and the TFT-CSDM beamforming in both relatively simple and complex underwater acoustic communication channels. Further, we verified low beamforming leakage from the proposed TFT-CPSD method. As the

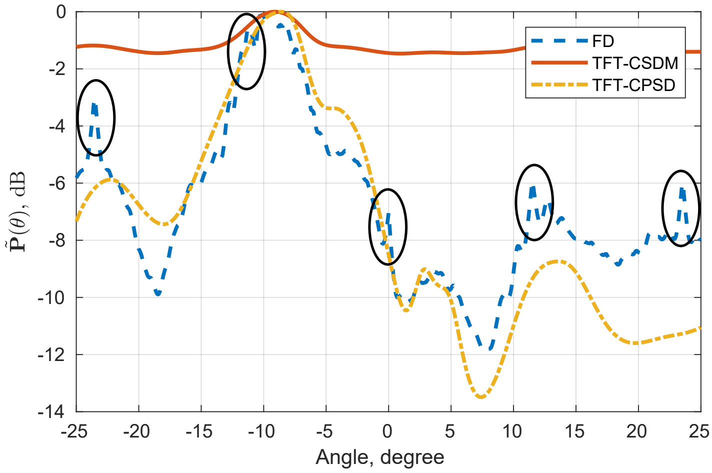

Figure 13: Comparisons of average spatial signal power $\widetilde{\mathrm{P}}(\theta)$ estimated from the DOA estimator using the three beamforming techniques with data from the simulation without adding noise in the channel. Beamforming leakage from the FD beamforming technique has been indicated in black circles, while the two TFT beamforming do not have such periodical leaking peaks.

proposed beamforming technique is based on the investigation of energy conservative (better than the TFT-CSDM beamforming) and energy leakage reduction (better than the FD beamforming), which is not relative to modulation schemes, thus it can be applied and tested with other modulation schemes apart from the OFDM schemes.

As the curvature of wave-front in shallow water is much more complicated than deep water transmission due to multipath and the gradient of sound, the channel can sometimes even be considered as sparse. In such case we may be unable to find a specific direction of arrival (DOA). To solve such a more complicated problem, a technique considering both the proposed TFT-CPSD beamforming as well as an adaptive sparse filter [4, 53] may need to be investigated in the following work. Besides, here we only consider one DOA session for each experiment session, while there might be multiple arrivals from different directions, then we need to consider a combining technique, e.g., maximum ratio combining, and an adaptive, e.g., angle-dependent, Doppler estimation technique. For such two techniques, readers are referred to the literature of [10] and [26]. The frame length investigated here may be specific for the experimental data collected in the northwest Pacific Ocean at a specific sea state. However, for the using of such proposed method, we suggest an investigation of the frame length with a test channel data prior to the application of it. Further, as we can see from Fig. 6, the DOA is not constant through the entire session and can experience a fluctuation of up to 3 degree. Considering such fluctuated DOA as a constant DOA may be an inferior way than fully tracking the actual DOA. As we can reduce the energy leakage by applying a proper way, either using the overlap-save or overlap-add or convolution methods, we expect that a DOA tracking algorithm considering the energy peak for each frame can be developed to improve the SNR and receiver performance.

Appendix A. Ambient noises correlation among hydrophone channels

Ambient noises on different receive hydrophone channels have often been assumed as uncorrelated and Gaussian distributed in UWA comunications [14, 15, 16, 17, 18, 19, 20], which is a simplified process of noise in real ocean scenarios. Kilfoyle et al. [21] pointed out that such simplification may significantly change the capacity value of channel spatial modulation. Here we present the cross-correlation of underwater ambient noise based on sea trial data measured by the vertical linear array (VLA) of different hydrophone channels to provide ocean acoustician an initial instruction on this issue.

To show the strength of linear relationship between two variables, the Pearson correlation coefficient [54] is used as

$$\xi = \frac{\sum_{k=1}^{K}(\varphi_1(k) - \bar{\varphi}_1)(\varphi_2(k) - \bar{\varphi}_2)}{\sqrt{\varepsilon_1^2}\sqrt{\varepsilon_2^2}}, \tag{A.1}$$

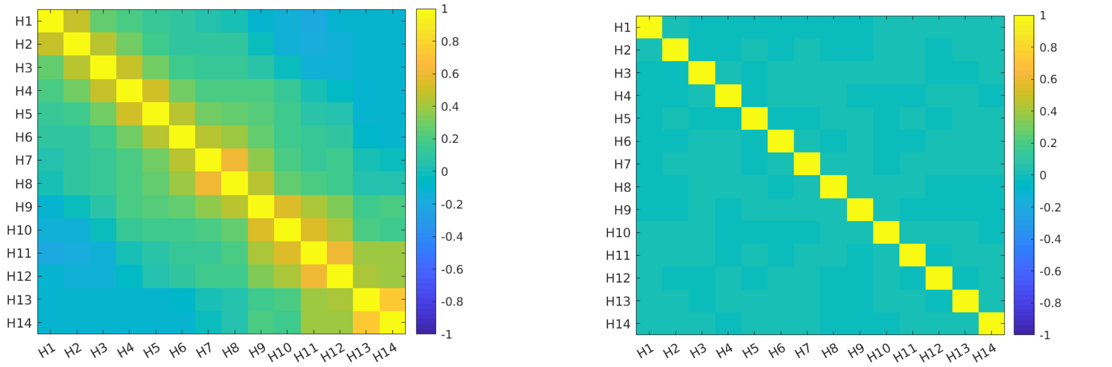

(a) Ambient noises measured by the VLA in the sea trial.

(b) Randomly distributed white Gaussian noise.

Figure A.14: Pearson correlation coefficient between different hydrophone channel noise in three cases. (a) Measured ambient noises in the sea trial; (b) White Gaussian noises. Negative correlations are in blue and positive correlations in yellow. 'H·' represents hydrophone index.

where

$$\varepsilon_1^2 = \sum_{k=1}^{K} (\varphi_1(k) - \bar{\varphi}_1)^2, \tag{A.2}$$

and

$$\varepsilon_2^2 = \sum_{k=1}^{K} (\varphi_2(k) - \bar{\varphi}_2)^2, \tag{A.3}$$

are covariance of the variables, $\varphi_1(k)$ and $\varphi_2(k)$ are the two variables, $\bar{\varphi}_1$ and $\bar{\varphi}_2$ are mean values of the two variables, respectively. Values between 0 and 0.3 (0 and -0.3) indicate a weak positive (negative) linear relationship via a shaky linear rule; values between 0.3 and 0.7 (-0.3 and -0.7) indicate a moderate positive (negative) linear relationship via a fuzzy-firm linear rule; and values between 0.7 and 1.0 (-0.7 and -1.0) indicate a strong positive (negative) linear relationship via a firm linear rule [54].

Before the sea trial communication sessions, we measured the ambient noise for each hydrophone channel at its depth (420 m + hydrophone distances [0 0.6 1.2 1.8 2.4 3.0 3.6 3.9 4.8 5.4 6.0 6.6 7.8 8.1] m) using the receive VLA. Fig. A.14(a) shows the overall Pearson correlation coefficients computed from (A.1) with 20 s measured ambient noise for all the 14 hydrophone channels. As a result, the positive correlation between ambient noises measured by two hydrophones gradually decreases from strong to weak as the distance between the two hydrophones increases. Ambient noises measured by different hydrophone channels show strong/moderate positive correlation from two neighbour hydrophones with distance less than 0.6 m, show week correlation when the distance between two hydrophones is from 0.6 m to 4.0 m, and can only be considered as uncorrected where and when the distance between two hydrophones is more than 4.0 m. For comparison, we also show the Pearson correlation coefficient of randomly distributed white Gaussian noise in Fig. A.14(b), which indicates uncorrected relationships between them.

As can be seen from Fig. A.14, when we add noise on the received signals for each hydrophone channel to obtain signals with target SNR for beamforming, we need to consider the specific measurement depth, position, and ocean bathymetry related correlation of channel ambient noise, to ensure the true capacity value of channel spatial modulation is obtained. Such specific correlation between channel noise makes influence on the beamforming performance. Detailed influence is out of the scope in this paper, and will be a research topic in the future work.

Acknowledgements

We would like to thank Dr. Yuriy V. Zakharov for his valuable help to improve this article. Funding for this work was provided by the European Unions Horizon 2020 research and innovation programme under the grant agreement number 654462 (STEMM-CCS).

References

[1] Z. Wang, S. Zhou, G. B. Giannakis, C. R. Berger, J. Huang, Frequency-domain oversampling for zero-padded OFDM in underwater acoustic communications, IEEE Journal of Oceanic Engineering 37 (1) (2011) 14–24. doi:10.1109/JOE.2011.2174070.

[2] S. Zhou, Z. Wang, OFDM for underwater acoustic communications, John Wiley & Sons, 2014.

[3] J. Li, P. R. White, J. M. Bull, T. G. Leighton, A noise impact assessment model for passive acoustic measurements of seabed gas fluxes, Ocean Engineering 183 (1) (2019) 294–304. doi:10.1016/j.oceaneng.2019.03.046.

[4] C. R. Berger, S. Zhou, J. C. Preisig, P. Willett, Sparse channel estimation for multicarrier underwater acoustic communication: From subspace methods to compressed sensing, IEEE Transactions on Signal Processing 58 (3) (2009) 1708–1721. doi:10.1109/TSP.2009.2038424.

[5] J. Li, P. R. White, B. Roche, Seafloor noise ensemble from vessel manoeuvre in the central North Sea, Ocean Engineering 196 (2020) 106836. doi:10.1016/j.oceaneng.2019.106836.

[6] J. Li, P. R. White, B. Roche, J. W. Davis, T. G. Leighton, Underwater radiated noise from hydrofoils in coastal water, J. Acoust. Soc. Am. 146 (5) (2019) 3552–3561. doi:10.1121/1.5134779.

[7] Y. Zhao, H. Yu, G. Wei, F. Ji, F. Chen, Parameter estimation of wideband underwater acoustic multipath channels based on fractional Fourier transform, IEEE Transactions on Signal Processing 64 (20) (2016) 5396–5408. doi:10.1109/TSP.2016.2582466.

[8] Z. Xu, Y. V. Zakharov, V. P. Kodanev, Space-time signal processing of OFDM signals in fast-varying underwater acoustic channel, in: IEEE OCEANS 2007-Aberdeen, UK, 2007, pp. 1–6. doi:10.1109/OCEANSE.2007.4302328.

[9] S. Ijaz, A. Silva, S. M. Jesus, Arrival-based equalizer for underwater communication systems, UCOMMS'12, Sestri Levante, Italy (2012) 1–10.

[10] J. Li, Y. V. Zakharov, Efficient use of space-time clustering for underwater acoustic communications, IEEE Journal of Oceanic Engineering 43 (1) (2018) 173–183. doi:10.1109/JOE.2017.2688558.

[11] B. Li, S. Zheng, F. Tong, Bit-error rate based Doppler estimation for shallow water acoustic OFDM communication, Ocean Engineering 182 (2019) 203–210. doi:10.1016/j.oceaneng.2019.04.045.

[12] T. Yang, A study of spatial processing gain in underwater acoustic communications, IEEE Journal of Oceanic Engineering 32 (3) (2007) 689–709. doi:10.1109/JOE.2007.897072.

[13] O. Hoshuyama, A. Sugiyama, A. Hirano, A robust adaptive beamformer with a blocking matrix using coefficient-constrained adaptive filters, IEICE Transactions on Fundamentals of Electronics, Communications and Computer Sciences 82 (4) (1999) 640–647.

[14] A. Rafati, H. Lou, C. Xiao, Soft-decision feedback turbo equalization for LDPC-coded MIMO underwater acoustic communications, IEEE Journal of Oceanic Engineering 39 (1) (2013) 90–99. doi:10.1109/JOE.2013.2241933.

[15] K. Pelekanakis, A. B. Baggeroer, Exploiting space–time–frequency diversity with MIMO–OFDM for underwater acoustic communications, IEEE Journal of Oceanic Engineering 36 (4) (2011) 502–513. doi:10.1109/JOE.2011.2165758.

[16] A. Song, A. Abdi, M. Badiey, P. Hursky, Experimental demonstration of underwater acoustic communication by vector sensors, IEEE Journal of Oceanic Engineering 36 (3) (2011) 454–461. doi:10.1109/JOE.2011.2133050.

[17] P. A. van Walree, F.-X. Socheleau, R. Otnes, T. Jenserud, The watermark benchmark for underwater acoustic modulation schemes, IEEE Journal of Oceanic Engineering 42 (4) (2017) 1007–1018. doi:10.1109/JOE.2017.2699078.

[18] S. E. Cho, H. C. Song, W. S. Hodgkiss, Successive interference cancellation for underwater acoustic communications, IEEE Journal of Oceanic Engineering 36 (4) (2011) 490–501. doi:10.1109/JOE.2011.2158014.

[19] S. Roy, T. M. Duman, V. McDonald, J. G. Proakis, High-rate communication for underwater acoustic channels using multiple transmitters and space–time coding: Receiver structures and experimental results, IEEE Journal of Oceanic Engineering 32 (3) (2007) 663–688. doi:10.1109/JOE.2007.899275.

[20] S. Kaddouri, P.-P. J. Beaujean, P.-J. Bouvet, G. Real, Least square and trended Doppler estimation in fading channel for high-frequency underwater acoustic communications, IEEE Journal of Oceanic Engineering 39 (1) (2013) 179–188. doi:10.1109/JOE.2013.2282065.

[21] D. B. Kilfoyle, J. C. Preisig, A. B. Baggeroer, Spatial modulation experiments in the underwater acoustic channel, IEEE Journal of Oceanic Engineering 30 (2) (2005) 406–415. doi:10.1109/JOE.2004.834168.

[22] Y. V. Zakharov, V. P. Kodanev, Experimental study of an underwater acoustic communication system with pseudonoise signals, Acoustical Physics 40 (5) (1994) 707–715. doi:10.1.1.324.1330.

[23] Y. V. Zakharov, A. K. Morozov, OFDM transmission without guard interval in fast-varying underwater acoustic channels, IEEE Journal of Oceanic Engineering 40 (1) (2015) 144–158. doi:10.1109/JOE.2013.2296842.

[24] C. Liu, Y. V. Zakharov, T. Chen, Doubly selective underwater acoustic channel model for a moving transmitter/receiver, IEEE Transactions on Vehicular Technology 61 (3) (2012) 938–950. doi:10.1109/TVT.2012.2187226.

[25] B. Henson, J. Li, Y. V. Zakharov, C. Liu, Waymark baseband underwater acoustic propagation model, in: Underwater Communications and Networking (UComms), IEEE, 2014, pp. 1–5. doi:10.1109/UComms.2014.7017132.

[26] J. Li, Y. V. Zakharov, B. Henson, Multibranch Autocorrelation Method for Doppler Estimation in Underwater Acoustic Channels, IEEE Journal of Oceanic Engineering 43 (4) (2018) 1099 – 1113. doi:10.1109/JOE.2017.2761478.

[27] J. G. Proakis, Digital communications. 1995, McGraw-Hill, New York.

[28] S. Haykin, J. H. Justice, N. L. Owsley, J. L. Yen, A. C. Kak, Array signal processing, Prentice-Hall, Inc., Englewood Cliffs, NJ, 1985.

[29] J. Li, P. Stoica, Z. Wang, On robust Capon beamforming and diagonal loading, IEEE Transactions on Signal Processing 51 (7) (2003) 1702–1715. doi:10.1109/TSP.2003.812831.

[30] J. L. Sutton, Underwater acoustic imaging, Proceedings of the IEEE 67 (4) (1979) 554–566. doi:10.1109/PROC.1979.11283.

[31] Z. Xu, H. Li, K. Yang, A Modified Differential Beamforming and Its Application for DOA Estimation of Low Frequency Underwater Signal, IEEE Sensors Journal (2020) 1–12doi:10.1109/JSEN.2020.2988025.

[32] E. Ozanich, P. Gerstoft, H. Niu, A feedforward neural network for direction-of-arrival estimation, The Journal of the Acoustical Society of America 147 (3) (2020) 2035–2048. doi:10.1121/10.0000944.

[33] K. J. Raghunath, U. V. Reddy, Finite data performance analysis of MVDR beamformer with and without spatial smoothing, IEEE Transactions on Signal Processing 40 (11) (1992) 2726–2736. doi:10.1109/78.165659.

[34] C. Vaidyanathan, K. M. Buckley, Performance analysis of the MVDR spatial spectrum estimator, IEEE Transactions on Signal Processing 43 (6) (1995) 1427–1437. doi:10.1109/78.388855.
[35] D. N. Swingler, A low-complexity MVDR beamformer for use with short observation times, IEEE Transactions on Signal Processing 47 (4) (1999) 1154–1160. doi:10.1109/78.752616.
[36] A. Quinquis, D. Boulinguez, Multipath channel identification with wavelet packets, IEEE Journal of Oceanic Engineering 22 (2) (1997) 342–346. doi:10.1109/48.585953.
[37] Y. Bai, J. Li, Y. Wu, Q. Wang, X. Zhang, Weighted Incoherent Signal Subspace Method for DOA Estimation on Wideband Colored Signals, IEEE Access 7 (2019) 1224–1233. doi:10.1109/ACCESS.2018.2886250.
[38] L. Ma, K. Dickson, J. McAllister, J. McCanny, QR decomposition-based matrix inversion for high performance embedded MIMO receivers, IEEE Transactions on Signal Processing 59 (4) (2011) 1858–1867. doi:10.1109/TSP.2011.2105485.
[39] J. Capon, High-resolution frequency-wavenumber spectrum analysis, Proceedings of the IEEE 57 (8) (1969) 1408–1418. doi:10.1109/PROC.1969.7278.
[40] S. T. Alexander, Adaptive signal processing: theory and applications, Springer-Verlag New York, Inc., 1986.
[41] S. Muramatsu, H. Kiya, Extended overlap-add and-save methods for multirate signal processing, IEEE transactions on Signal Processing 45 (9) (1997) 2376–2380. doi:10.1109/78.622960.
[42] A. Daher, E. H. Baghious, G. Burel, E. Radoi, Overlap-save and overlap-add filters: Optimal design and comparison, IEEE Transactions on Signal Processing 58 (6) (2010) 3066–3075. doi:10.1109/TSP.2010.2044260.
[43] P. Welch, The use of fast Fourier transform for the estimation of power spectra: a method based on time averaging over short, modified periodograms, IEEE Transactions on audio and electroacoustics 15 (2) (1967) 70–73.
[44] A. V. Oppenheim, J. R. Buck, R. W. Schafer, Discrete-time signal processing. Vol. 2, Upper Saddle River, NJ: Prentice Hall, 2001.
[45] L. Pizzuti, C. dos Santos Guimarães, E. G. Iocca, P. H. S. de Carvalho, C. A. Martins, Continuous analysis of the acoustic marine noise: A graphic language approach, Ocean Engineering 49 (2012) 56–65. doi:10.1016/j.oceaneng.2012.04.004.
[46] D. Wittekind, M. Schuster, Propeller cavitation noise and background noise in the sea, Ocean Engineering 120 (2016) 116–121. doi:10.1016/j.oceaneng.2015.12.060.
[47] R. P. Hodges, Underwater acoustics: Analysis, design and performance of sonar, John Wiley & Sons, 2011. doi:10.1002/9780470665244.
[48] P. Asolkar, A. Das, S. Gajre, Y. Joshi, Comprehensive correlation of ocean ambient noise with sea surface parameters, Ocean Engineering 138 (2017) 170–178. doi:10.1016/j.oceaneng.2017.04.033.
[49] J. Liu, I. Lin, C. Chu, Effects of sediment properties on surface-generated ambient noise in a shallow ocean, Ocean Engineering 32 (16) (2005) 1887–1905. doi:10.1016/j.oceaneng.2005.04.001.
[50] D.-Q. Li, J. Hallander, T. Johansson, Predicting underwater radiated noise of a full scale ship with model testing and numerical methods, Ocean Engineering 161 (2018) 121–135. doi:10.1016/j.oceaneng.2018.03.027.
[51] A. Brooker, V. Humphrey, Measurement of radiated underwater noise from a small research vessel in shallow water, Ocean Engineering 120 (2016) 182–189. doi:10.1016/j.oceaneng.2015.09.048.
[52] P. Kellett, O. Turan, A. Incecik, A study of numerical ship underwater noise prediction, Ocean Engineering 66 (2013) 113–120. doi:10.1016/j.oceaneng.2013.04.006.
[53] Z. Tang, G. Blacquiere, G. Leus, Aliasing-free wideband beamforming using sparse signal representation, IEEE Transactions on Signal Processing 59 (7) (2011) 3464–3469. doi:10.1109/TSP.2011.2140108.
[54] J. Benesty, J. Chen, Y. Huang, I. Cohen, Pearson correlation coefficient, in: Noise reduction in speech processing, Springer, 2009, pp. 1–4.